

# Sources of contamination to weak lensing tomography: redshift-dependent shear measurement bias

Elisabetta Semboloni<sup>1,2</sup>;<sup>?</sup> Ismael Tereno<sup>1</sup>, Ludovic van Waerbeke<sup>2</sup>, Catherine Heymans<sup>2,3</sup>

<sup>1</sup> Argelander-Institut für Astronomie, Auf dem Hügel 71, Bonn, D-53121, Germany.

<sup>2</sup> University of British Columbia, Department of Physics & Astronomy, 6224, Agricultural Road, Vancouver, B. C., V6T, Canada.

<sup>3</sup> Institute for Astronomy, University of Edinburgh, Royal Observatory, Blackford Hill, Edinburgh, EH9 3HJ, UK.

21 February 2024

## ABSTRACT

The current methods available to estimate gravitational shear from astronomical images of galaxies introduce systematic errors which can affect the accuracy of weak lensing cosmological constraints. We study the impact of KSB shape measurement bias on the cosmological interpretation of tomographic two-point weak lensing shear statistics.

We use a set of realistic image simulations produced by the STEP collaboration to derive shape measurement bias as a function of redshift. We define biased two-point weak lensing statistics and perform a likelihood analysis for two fiducial surveys. We present a derivation of the covariance matrix for tomography in real space and a fitting formula to calibrate it for non-Gaussianity.

We find the biased aperture mass dispersion is reduced by  $\sim 20\%$  at redshift  $z=1$ , and has a shallower scaling with redshift. This effect, if ignored in data analyses, biases  $\sigma_8$  and  $w_0$  estimates by a few percent. The power of tomography is significantly reduced when marginalising over a range of realistic shape measurement biases. For a CFHTLS-Wide-like survey,  $[\sigma_m; \sigma_8]$  confidence regions are degraded by a factor of 2, whereas for a KIDS-like survey the factor is 3.5. Our results are strictly valid only for KSB methods but they demonstrate the need to marginalise over a redshift-dependent shape measurement bias in all future cosmological analyses.

**Key words:** Gravitational lensing - large-scale structure of the Universe - cosmological parameters

## 1 INTRODUCTION

Weak gravitational lensing by large-scale structure, or cosmic shear (see Munshi et al. 2008 for a review), is a powerful tool to investigate dark energy and the large-scale distribution of dark matter (Albrecht et al. 2006; Peacock et al. 2006). In the last decade, two-point shear statistics have been successfully measured and used to constrain parameters of the matter power spectrum (from the early constraints of van Waerbeke et al. 2001 to the recent results of Fu et al. 2008) and dark energy (Jarvis et al. 2006; Hoekstra et al. 2006; Semboloni et al. 2006; Schimd et al. 2007; Kilbinger et al. 2008).

The information contained in the cosmic shear signal is more efficiently exploited if the redshift of the source galaxies is available. In particular, the measurement of shear statistics in redshift bins, or tomographic weak lensing, can greatly improve cosmological constraints (Hu 1999), especially for dark energy (Takada &

Jain 2004), since the weak lensing signal scales differently with redshift for different models of dark energy evolution.

The accuracy of cosmic shear constraints is affected by systematic effects. Systematics arise primarily from intrinsic alignments, redshifts uncertainties, and shear measurement errors. Intrinsic alignments are non-cosmological sources of shear correlation, caused by an intrinsic correlation between the orientation of galaxies (Crittenden et al. 2001) or by shear-shape correlation, i.e., by a correlation between galaxies shapes and surrounding density fields (Hirata & Seljak 2004). These effects have been modeled, eg., in Heymans et al. (2006b) and have also been constrained with data (Mandelbaum et al. 2006). In particular, it has been shown (Hirata et al. 2007; Bridle & King 2007) that ignoring the effect of the shear-shape correlation on the amplitude of the two-point shear statistics heavily biases the constraints on the equation of state of dark energy. The impact of redshifts uncertainties on cosmic shear has also been analysed in several studies (Ishak & Hirata 2005; Ma, Hu & Huterer 2006; van Waerbeke et al. 2006).

This paper deals with the third primary effect: shear measure-

<sup>?</sup> sembolon@astro.uni-bonn.de

ment errors due to the lack of an unbiased method to estimate gravitational shear from astronomical images of galaxies. It aims to derive the effect of shear measurement bias on dark energy constraints both with and without tomography. The estimation of gravitational shear is technically challenging and the methods available today do not seem to do better than the percent level of accuracy. The Shear Testing Programme (STEP), and more recently the gravitational lensing estimation accuracy test (GREAT08) (Bridle et al. 2008), represent to date the largest collaborations aimed at testing and improving the accuracy of the existing shear measurement methods with the use of realistic sets of simulated images. Current methods are based on the KSB approach (Kaiser, Squires & Broadhurst 1995; Luppino & Kaiser 1997), shapelet decomposition (Bernstein & Jarvis 2002; Réfrégier & Bacon 2003; Kuijken 2006), or Bayesian techniques (Kitching et al. 2008b). The STEP collaboration has shown that the methods developed in the past years underestimate on average the shear signal by a few percent (Heymans et al. 2006a; Massey et al. 2007), implying the measurement of two-point shear statistics is underestimated by two to ten percent. Moreover, the STEP collaboration showed that this bias is not constant but depends on the brightness and size of the galaxies. Indeed, for most methods the measured shear is overestimated for bright galaxies and greatly underestimated for faint galaxies. This may be a limitation of the accuracy with which one can derive cosmological constraints using cosmic shear statistics in future ground-based and space-based astronomical surveys such as KIDS, LSST, Pan-STARRS, DES, JDEM or EUCLID.

There are in the literature various studies dealing with the impact of shear measurement errors and PSF modeling on cosmic shear measurements (Hirata & Seljak 2003; Hoekstra 2004; van Waerbeke et al. 2005; Jain, Jarvis & Bernstein 2006; Paulin-Henriksson et al. 2008). There are also several cosmic shear forecasts of cosmological parameters which include and model generic types of systematic errors, such as multiplicative and additive errors in shear measurements (Huterer et al. 2006; Amara & Réfrégier 2007; Kitching, Taylor & Heavens 2008a). In these previous works the bias has been assumed to be a generic function of the redshift; in this paper we adopt a different approach, consisting in explicitly quantifying the bias as a function of redshift using realistic simulations, as opposed to using generic modeling. In order to derive the expression of the bias as a function of redshift we reanalyse the STEP2 simulations using a KSB pipeline. We observe that the bias depends on the characteristics of the galaxies such as magnitude and size and we use these dependencies to derive a realistic expression of the bias as a function of redshift. In order to evaluate the impact of this bias on the estimation of cosmological parameters we perform a likelihood analysis of tomographic two-point cosmic shear in a space of cosmological and bias parameters, including small-scale non-Gaussian corrections in the covariance matrix. We note that even though we model the bias using a particular implementation of KSB, the results we find are general as all KSB methods tested by the STEP collaboration show the same behavior.

The paper is organized as follows: in Section 2 we describe the results of the STEP2 analysis and the procedure to estimate the bias as a function of redshift. Section 3 defines the tomographic two-point shear statistics in the presence of a redshift-dependent bias. In Section 4 we define the space of cosmological and shear measurement bias parameters where the likelihood analysis will be performed. Section 5 presents the correction for non-Gaussianity to be applied to the covariance matrix of tomographic two-point correlation functions computed for a Gaussian shear field. The derivation of this covariance in the real space is detailed in the Appendix.

The results of the likelihood analysis are presented and discussed in Section 6 and we conclude in Section 7.

## 2 STEP2 ANALYSIS

In the last decade a large effort has been made in order to establish the accuracy with which one can estimate shear from images of galaxies. The Shear Testing Programme is a collaboration which aims to test and improve methods for PSF correction using realistic sets of simulations. The STEP1 and STEP2 simulations have a depth similar to the images of the CFHTLS-Wide survey, which is to date the largest deep weak lensing survey available. The results of the analyses on the simulations can thus be immediately used to assess the accuracy on the cosmological constraints from real surveys. The galaxies in the STEP2 set of simulations have a brightness profile built using a shapelets decomposition of galaxies observed with the Hubble Space Telescope (Massey et al. 2004); the resulting profiles are more realistic than the STEP1 simulations in which elliptical galaxies are characterised by de Vaucouleurs profiles and spiral galaxies are characterised by a bulge and a projected disk.

We recall here the main characteristics of the STEP2 simulations referring the reader to Massey et al. (2007) for further information. The STEP2 set of simulations is composed of six subsets, each characterised by a different PSF. Each subset is identified by an alphabetical letter from A to F. The PSFs A B and C are typical Subaru PSFs. The PSF D and E are highly elliptical, aligned along the  $x$  and  $y$  axis, respectively. The PSF F is a circularly symmetric PSF. Furthermore the PSF is constant across the field; the seeing size is  $0.6$  arcsec, apart from PSF C for which the seeing is  $0.8$  arcsec. For each PSF there are 64 pairs of  $7^0 - 7^0$  images with pixel size of  $0.206$  arcsec. Each pair corresponds to one image and its rotation by 90 degrees. A shear field and a PSF are applied to the image pairs. The image pairs have been generated so that one can estimate the shear using a galaxy and its rotated pair, reducing the effect of shape noise on the measured shear. The STEP2 simulations are therefore more suitable for our study than the STEP1 simulations both because the galaxy profiles are more realistic and the bias can be determined to a higher level of accuracy. For this reason we will consider the STEP2 set of simulations as our main dataset, but we will briefly discuss the results we obtain using the STEP1 set of simulations at the end of this section.

We analyse the STEP2 simulations using the KSB implementation used in Fu et al. 2008 but with the following significant changes:

- we do not introduce a weighting scheme, i.e. all the objects have the same weight

- we use the trace of the shear polarizability tensor  $\mathcal{P}_g$  in the shear estimator for each object

- we select objects only according to their signal-to-noise ratio. The signal-to-noise is defined by the  $\text{snr}$  parameter provided by the IMCAT<sup>1</sup> shape measurement software.

We introduce these modifications as we want to keep the PSF correction method as basic as possible avoiding arbitrary “ad hoc” choices which might change the results significantly. For each PSF, we analyse the 64 pairs of images, merging the catalogues of the image pairs so that the final catalogue is free of spurious detections.

<sup>1</sup> <http://www.ifa.hawaii.edu/~kaiser/>, developed by Nick Kaiser.

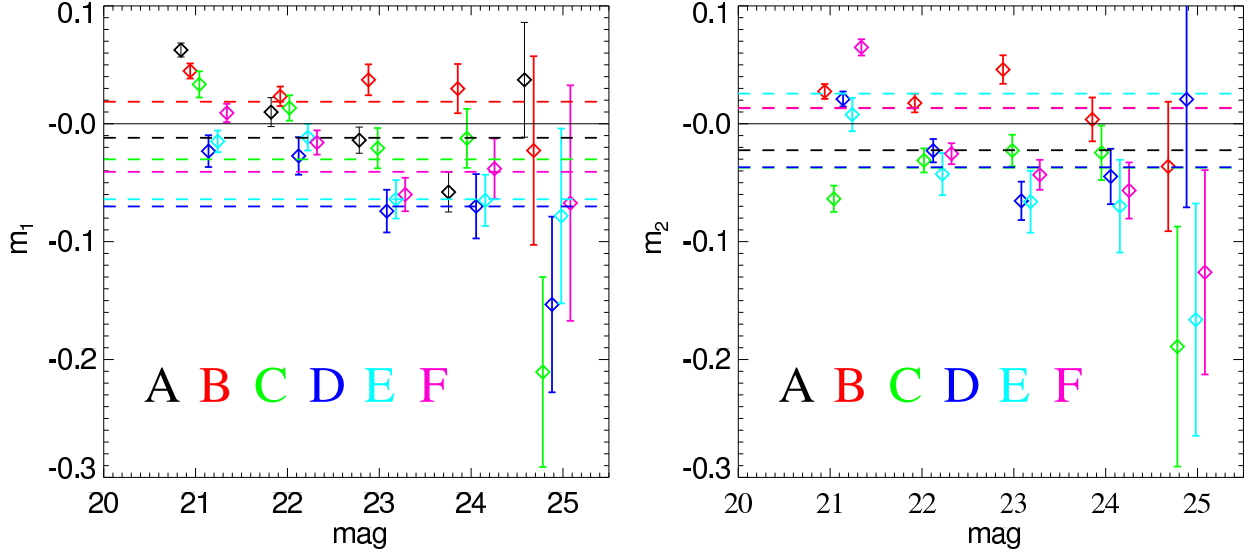


**Figure 1.** Left panel: values of the multiplicative bias  $m_1$  as a function of magnitude averaged on the 64 image pairs. Error bars represent the standard deviations around the average value. Different colors refer to different PSF sets. The dashed lines show the values of the multiplicative bias factor  $m_1$  averaged on the whole catalogue. Right panel: same as the left panel but for the second component  $m_2$ .

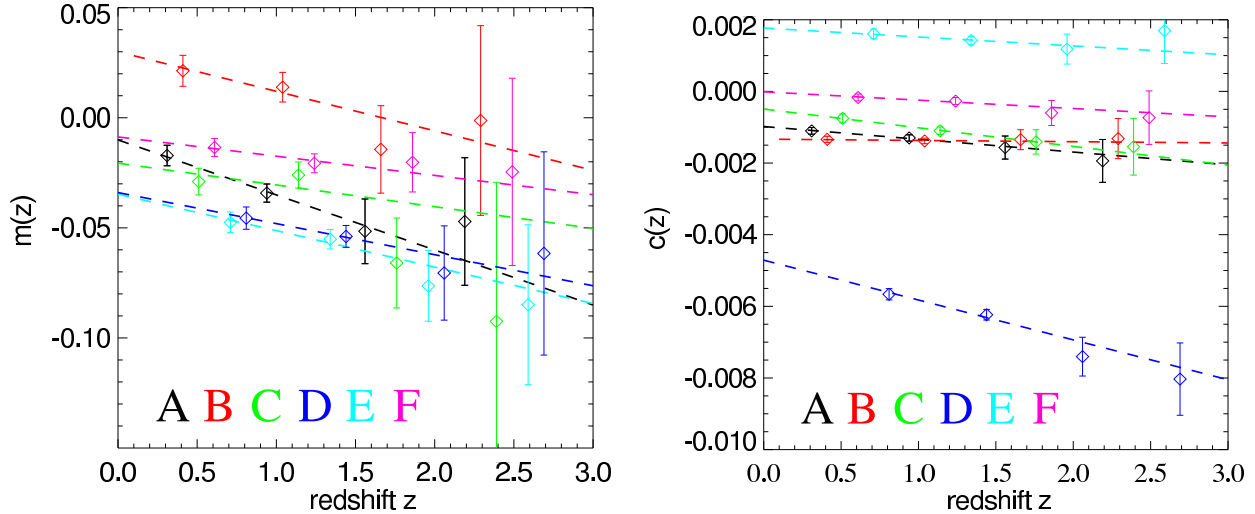


**Figure 2.** Left panel: average value of the multiplicative bias factor  $m$  as a function of the redshift for each set of PSF. The value has been obtained by averaging over the one hundred bootstrap realisations built as indicated in the text. Error bars represent standard deviations of the one hundred realisations. The dashed lines represent the best linear fit to the points. Right panel: same as the left panel for the additive bias constant  $c$ .

As suggested in Massey et al. (2007) we describe the difference between the measured shear  $\gamma$  and the input shear signal  $\gamma_{\text{true}}$  using the multiplicative  $m = (m_1; m_2)$  and additive  $c = (c_1; c_2)$  bias factors:

$$\gamma_i(z) = \gamma_{i,\text{true}}(z) + m_i \gamma_{i,\text{true}}(z) + c_i \quad i = 1, 2 \quad (1)$$

The estimated shear at a position  $\theta$  is affected by a multiplicative bias  $m$ . The main reason for this calibration error is that KSB methods do not completely correct for the isotropic kernel of the PSF, leaving thus a residual which is seeing and magnitude dependent. Since the seeing in the STEP2 simulations is constant across the image,  $m$  is independent of position. The additive bias  $c$  comes from incomplete correction of the PSF anisotropy. This originates from the approximative nature of the KSB method and also from the residuals due to the modeling of the variation of the PSF across the image, which depend on the distribution of the observed stars.

The obtained  $m$  and  $c$  biases depend on the magnitude and on the size of the galaxies. We define the size of an object as the characteristic size  $r_h$  of the Gaussian profile which best fit the brightness profile as defined by the IMCAT software. We verify that our results are similar to those obtained by STEP2 by measuring the values of  $m$  and  $c$  as a function of magnitude for the two ellipticity components (see Fig. 1). For example, the value of the  $m$  components averaged over all galaxies lies between  $-7\%$  and  $+2\%$  depending on the PSF subset, with a mean over PSFs of  $-3\%$ .

We want now to convert the bias as a function of magnitude and size into a bias as a function of redshift. To do so, we need to find the average redshift distribution of the galaxies belonging to each size and magnitude bin, using the CFHTLS-Deep photometric redshift catalogue (Ilbert et al. 2006). For this we first convert the STEP2 magnitudes into the corresponding CFHTLS-Deep values.

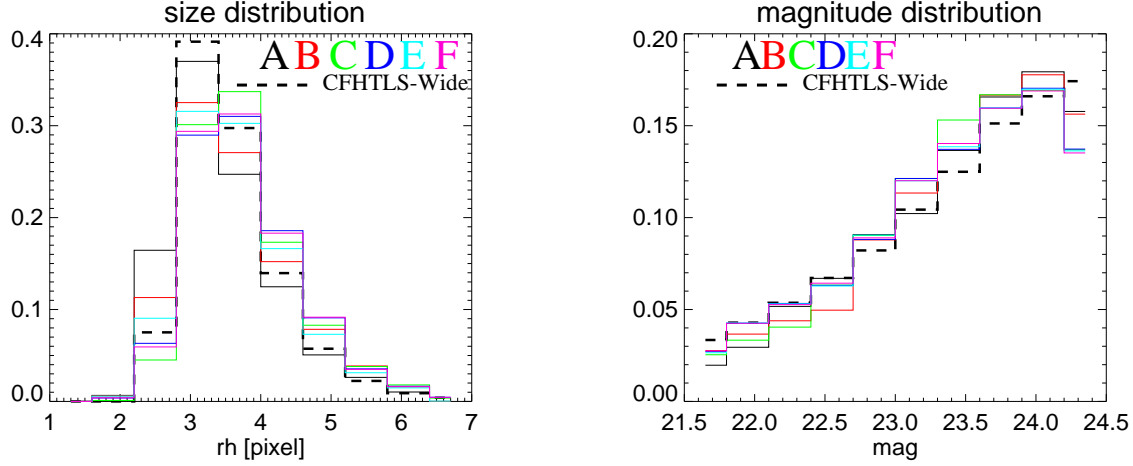


**Figure 3.** Left panel: size distribution of the galaxies in each of the STEP2 sets (solid histograms). The distribution of sizes of the CFHTLS-Wide galaxies is shown for comparison (dashed histogram). The size of the galaxies in the CFHTLS Deep catalogue have been converted into the STEP2 simulations pixel units of 0.206 arcsec. Right panel: distribution of magnitudes for each of the STEP2 PSF sets (solid) and for the CFHTLS-Wide galaxies (dashed).

**Table 1.** Best-fit values of the redshift bias parameters  $a_m$ ,  $b_m$ ,  $a_c$ ,  $b_c$  and their relative errors for each PSF set of the STEP2 simulations. These values are used to plot the lines shown in Figure 2. The last line shows the averages over all PSFs.

PSF	$a_m$ ( $10^{-2}$ )		$b_m$ ( $10^{-1}$ )		$a_c$ ( $10^{-4}$ )		$b_c$ ( $10^{-4}$ )	
A	2.5	0.7	0.10	0.06	3.5	1.4	9.8	1.3
B	1.8	1.1	0.28	0.09	0.4	1.0	13.1	1.2
C	1.0	1.0	0.23	0.08	5.2	2.0	6.0	1.7
D	1.4	1.0	0.41	0.07	11.1	2.7	52.6	2.2
E	1.7	0.8	0.41	0.06	2.5	2.3	16.7	1.9
F	0.9	0.7	0.11	0.06	2.3	1.7	0.8	1.3
mean	1.6	0.4	0.02	0.03	4.2	0.8	10.9	0.7

This is done by simply adding the photometric zero-point specified in the header of the images. We then find the conversion between the observed size of an object in each set of simulations and the size it would have in the CFHTLS-Deep catalogues. A conversion is needed because the pre-seeing size is the reference size which one should use to compare populations of galaxies between catalogues with different seeing. This is in principle not straightforward because the observed size depends on the seeing through a convolution. We check the difference of the seeing values comparing the locus of the stars in the simulations and in the CFHTLS-Deep catalogues. To do this we express the size of the stars in the CFHTLS Deep catalogue in units of pixels of the STEP2 simulations (the pixel size of the STEP2 simulations is 0.206 arcsec whereas the pixel size of the CFHTLS images is 0.186 arcsec). We find that the difference between the star size in each set of simulations and the star size in the CFHTLS-Deep catalogue is always smaller than 1=5 pixels except for the PSF C where the difference is about half a pixel. From this, we conclude that we do not need to reassign the size of the STEP2 galaxies.

We chose a magnitude range  $21.5 < \text{mag} < 24.5$ , for which a survey with the same depth of the simulations is complete. We divide the galaxies in bins of size and magnitude. By the definition (Eq. 1),  $m$  and  $c$  are two-dimensional vectors but for our purposes we set both components equal to the average between the two components and define scalar quantities:  $m = \frac{1}{2}(m_1 + m_2)$  and  $c = \frac{1}{2}(c_1 + c_2)$ . For each bin,  $i$ , containing  $n_i$  galaxies, we

compute the average bias parameters  $m_i$  and  $c_i$  and respective uncertainties  $\sigma_{m_i}$  and  $\sigma_{c_i}$ . We divide the CFHTLS-Deep catalogue into the same magnitude-size bins. Each galaxy in the simulation is assigned a value  $m_j$  and  $c_j$ , extracted from two Gaussians of mean  $m_i$  and  $c_i$  and dispersion  $\sigma_{m_i}$  and  $\sigma_{c_i}$ , and a redshift  $z_j$  extracted randomly from the CFHTLS-Deep galaxies belonging to the same bin. We bin the result in redshift bins  $z_k$ , and the total bias in each redshift bin  $z_k$  is given by:

$$m(z_k) = \frac{\sum_{j=1}^{n_k} m_j}{n_k}; \quad c(z_k) = \frac{\sum_{j=1}^{n_k} c_j}{n_k} \quad (2)$$

where  $n_k$  is the number of galaxies in the redshift bin. We repeat this procedure one hundred times. The final value of  $m(z)$  and  $c(z)$  and the relative errors are obtained averaging over the one hundred realisations.

We chose to fit  $m(z)$  and  $c(z)$  using a linear function:

$$m(z) = a_m z + b_m; \quad c(z) = a_c z + b_c \quad (3)$$

We perform the fit using only objects with redshifts  $z < 2.5$ . We show the values of the multiplicative and additive biases as a function of the redshift in Figure 2 where the best linear fit to the data is also shown. The best-fit parameter values and relative errors are summarized in Table 1. Overall the shear is generally underestimated by a few percent. The multiplicative bias parameter  $m(z)$  has a negative slope  $a_m$  which is roughly 1-2% for all the PSF types. The additive constant  $c(z)$  shows a slope which is consistent with zero except for PSF D. The value of the constant  $b_c$  is also significant in particular for PSF D and E. We repeated the analysis assuming the bias to depend only on the magnitude, i.e., dividing the catalogue only in bins of magnitude, and found similar results for the functions  $m(z)$  and  $c(z)$ . This is due to the fact that the size distribution as a function of redshift does not change significantly, so even though the bias slightly depends on the size the average bias is roughly the same for each redshift bin.

One should expect the values of the bias parameters to change if the selection criteria change. For example, including low signal-to-noise objects increases the overall bias and also affects the dependence on redshift,  $a_m$ . In order to explore pessimistic cases we removed the signal-to-noise threshold (spurious detections are still removed by merging each object with its rotated companion). The

biases increase significantly. The mean  $m$  over all PSFs is now larger than 10%, whereas the redshift-dependence has a slope  $a_m$  between 6% and 4%, depending on the PSF. This is a consequence of the fact that lowering the signal-to-noise threshold we include in the final catalogues a larger number of faint objects which are preferentially at high redshifts. This result shows that when using simulations to find a recalibrating factor, capable of compensating an average shear measurement bias, the factor obtained can only be safely applied to a similar population of galaxies. Likewise, our results are only strictly valid for surveys with size and magnitude distributions similar to the STEP2 catalogue. As we already mentioned, this is likely to be the case for the CFHTLS-Wide, which has a similar depth to the STEP2 simulations. We show in Figure 3 that the size and magnitude distributions of STEP2 indeed match those of the CFHTLS-Wide.

We analysed the STEP1 sets of simulations and derived their redshift-dependent biases. We notice that the distribution of galaxies in STEP1 includes a higher fraction of large galaxies than real data for the same depth such as the CFHTLS-Wide data. We find that the average multiplicative bias is 2%, averaged over the PSFs subsets with much less dispersion between PSFs than for STEP2. It is characterised by a slope value  $a_m$  always smaller than 1%, indicating that the accuracy of the shape measurement degrades less rapidly when the signal-to-noise ratio decreases in comparison to the STEP2 simulations.

The analysis of STEP1 and STEP2 simulations give the same qualitative results: the average bias is negative and the bias increases with redshift. The amplitude of the bias measured in the STEP1 simulations is smaller than the bias in the STEP2 simulations. The difference in the results is not surprising as the shape and the amplitude of the measured bias depends on the characteristics of the simulations. We conclude that in order to quantify the effect of the bias on real data one should use simulations that are as realistic as possible and as we already pointed out the STEP2 simulations are more realistic than the STEP1 simulations.

### 3 GRAVITATIONAL LENSING STATISTICS

In the next sections we explore the impact of the shear bias on cosmological constraints obtained with two-point shear statistics, both with and without considering redshift binning. To do so we derive an expression for two-point shear statistics which include the redshift-dependent bias of the shape measurement.

From Eq. (1), the measured correlation function is related to the true correlation function via

$$h(\theta) = h[1 + m(z)][1 + m(z^0)]_{\text{true}}(\theta) + h_c(z) c(z^0) \quad (4)$$

Since the two types of biases,  $m$  and  $c$ , are independent there are no mixed terms in Eq. (4). The first term of the right-hand side is identical to the correlation function,  $h_{\text{mod}}(\theta)$ , of a modified convergence  $m_{\text{od}} = (1 + m)_{\text{true}}$ . The power spectrum of the modified convergence relates to the matter power spectrum. Using the Limber approximation (Bartelmann & Schneider 2001), the relation is:

$$P(s) = \frac{9}{4} \frac{2}{m} \left( \frac{H_0}{c} \right)^4 \int_0^{z_{\text{sup}}} dw \frac{G_i(w) G_j(w)}{a^2(w)} P\left(\frac{s}{f_K(w)}; w\right); \quad (5)$$

with

$$G_i(w) = \int_{w^0}^{w^0(z_{\text{sup}})} dw^0 [1 + m(w^0(z))] p_{w,i}(w^0) \frac{f_K(w^0/w)}{f_K(w^0)}; \quad (6)$$

$f_K(w)$  is the comoving angular-diameter distance and  $m(w)$  is the multiplicative bias written as a function of the comoving distance  $w$ . Eqs. (5) and (6) take into account tomography, describing auto- and cross-correlations between redshift bins  $[z_{\text{inf}}, z_{\text{sup}}]$  where the distribution of the sources  $p_{w,i}(w)$  is zero for  $w < w(z_{\text{inf}})$  and  $w > w(z_{\text{sup}})$ . Notice the effect of the multiplicative redshift-dependent bias is equivalent to a change in the source redshift distribution. Since  $1 + m(z)$  is a decreasing function (cf. Fig. 2), the effective redshift distribution is shallower.

The modified two-point shear measured in apertures can be computed as usual, by integrating the shear-shear correlation function, Eq. (1), with the appropriate filters. For the top-hat variance at an angular scale  $\theta$  we obtain

$$\begin{aligned} h^2(\theta) = & 2 \int_0^1 ds s P(s) [W_1(s\theta)]^2 + \\ & + \frac{1}{2\theta^4} \int_0^\theta d^2 \int_0^\theta d^2 \left[ \int_{w(z_{\text{inf}})}^{w(z_{\text{sup}})} dw p_w(w) \right. \\ & \left. \int_{w^0(z_{\text{inf}})}^{w^0(z_{\text{sup}})} dw^0 p_w^0(w^0) h_c(w(z)) c(w^0(z)) \right]; \quad (7) \end{aligned}$$

The first term integrates the modified convergence power spectrum, Eq. (5), using the top-hat filter in Fourier space,  $W_1(\theta) = J_1(\theta)/\theta$ , where  $J_1(\theta)$  is the Bessel function of first order. The second term of Eq. (7) is the contribution from the additive bias. It is the integral in the aperture of the second term of Eq. (1), using the top-hat filter in the real space. Notice that due to the redshift dependence of  $c$  the integral over the aperture also includes an integration in the radial direction, weighted by the source distribution. If the correlation  $h_c(z) c(z^0)$  is constant across the image, the effect of the additive redshift-dependent bias is to add a constant to the two-point shear statistics.

Similarly, the variance of the aperture mass is

$$hM_{\text{ap}}^2(\theta) = 2 \int_0^1 ds s P(s) [W_2(s\theta)]^2; \quad (8)$$

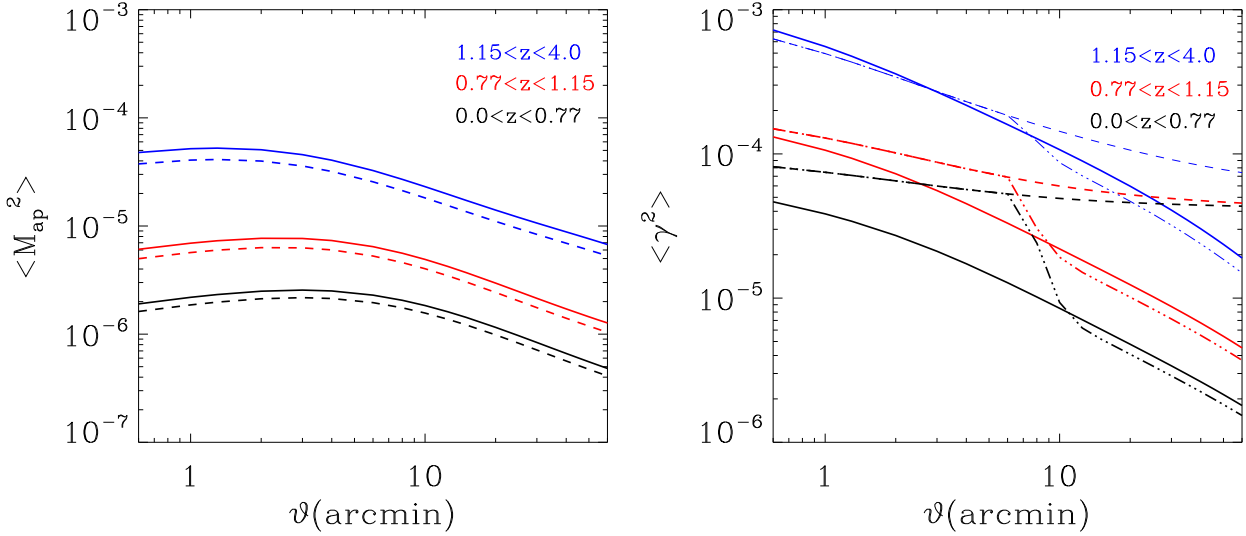
with  $W_2(\theta) = 12 J_4(\theta)/\theta^2$ , where  $J_4(\theta)$  is the Bessel function of fourth order. In this case there is no contribution from the additive bias because the filter of the aperture mass dispersion in real space is a compensated filter and thus insensitive to a constant shear.

Figure 4 shows biased and unbiased two-point shear statistics for three redshift bins. Only the three auto-correlations are shown. For this example we plot Eqs. (7) and (8) using a cosmological fiducial model, and bias parameters similar to PSF D and E, which are the most extreme cases. We parameterise the distribution of the sources,  $p_w(w)$ , as in Benjamin et al. (2007)

$$p(z) = \frac{1}{N} \frac{z}{z + z_0} \quad (9)$$

normalized to 1, with  $z_0 = 0.73$ ;  $z_0 = 4.52$ ;  $z_0 = 0.80$ , corresponding to a median redshift  $z_m = 0.77$ . These values were derived by fitting the density of galaxies  $n_k$  found in Section 2 for each PSF, using only galaxies with  $z < 2.5$ . We find similar results for all PSFs.

The left panel of Fig. 4 shows that the modified aperture mass variance decreases by a scale independent factor of 15% to 30%,



**Figure 4.** Biased and unbiased two-point shear statistics as function of angular scale  $\theta$  for three redshift bins. The unbiased signal (solid lines) is compared with the signal that would be measured on a survey with very elliptical PSF (dashed lines) characterised by the following bias parameters:  $a_m = 0.03$ ,  $b_m = 0.06$ ,  $a_c = 0.001$ ,  $b_c = 0.006$ . Left panel: for  $M_{ap}^2(\theta)$ . Right panel: for the top-hat variance  $\gamma^2(\theta)$ . The extra lines (dash-dotted) show a case where the additive bias only correlates on small scales. See text for details.

increasing with redshift. This increase produces a shallower scaling of the amplitude of  $M_{ap}^2(\theta; z)$  with the redshift. Modeling the redshift scaling with a power law we find it changes as:

$$\begin{aligned} M_{ap}^2(\theta) &\propto z^{2.05} \quad (\text{no bias}) \\ M_{ap}^2(\theta) &\propto z^{1.95} \quad (a_m = 0.03; b_m = 0.06): \end{aligned}$$

The right panel of Fig. 4 shows that the top-hat variance is dominated by the additive constant. Indeed, assuming the additive bias is constant across the image and correlates at all scales, the second term of the right-hand side of Eq. (7) writes

$$C = \left[ \int_{w(z_{inf})}^{w(z_{sup})} dw \, c(w(z)) \, p_w(w) \right]^2 : \quad (10)$$

A constant bias of  $b_c \approx 10^{-3}$ , which is the average value between the PSFs shown in the Table 1, yields  $C \approx 10^{-6}$  which is significant when compared to the cosmic shear signal, especially at the lower redshift bins, invalidating any cosmological interpretation. This is in agreement with Huterer et al. (2006) where it was found that an additive bias larger than  $10^{-4}$  would degrade the cosmological constraints of future weak lensing probes. This result suggests that whenever the PSF is not well corrected and the residual is constant aperture mass statistics should be preferred.

We show in the right panel of Figure 4 a more realistic case of modified top-hat variance, which assumes the PSF is modeled independently in sub-regions of the image. In this case, the additive bias only correlates at the scales of those sub-regions. In this example we assume the correlation is constant below  $\theta^0$ , which is a typical scale of the CCDs of ground-based cameras, and decreases steeply (exponentially) to zero at larger scales. In this toy-model the PSF residuals are strongly correlated at small scales enhancing strongly the signal, whereas on large scales  $\theta > \theta^0$  the PSF residuals are decorrelated and only the multiplicative constant affects the signal. We expect something similar to happen on real data as the PSF varies across the field and it is generally corrected by interpolating the PSF shape over a characteristic area. If this is the case, the additive constant would affect both the top-hat and the aperture mass variances and the effect could be significant at small

scales. However, the STEP2 simulations have a PSF which is constant across the field of view and this does not allow one to explore in more detail the effect of such a residual on real data.

#### 4 PARAMETER SPACE DEFINITION

In order to estimate the impact of the redshift-dependent shear measurement bias on cosmological constraints, we perform a likelihood analysis in a nine-dimensional grid using two-point shear statistics with and without tomography.

We define the log-likelihood of a model as

$$\begin{aligned} L(\theta) = \frac{1}{2} & [d_{ij}(\theta) - v_{ij}(\theta; \gamma)]^T C(\theta; \gamma^0; \gamma)^{-1} \\ & [d_{ij}(\theta^0) - v_{ij}(\theta^0; \gamma)] : \end{aligned} \quad (11)$$

Both the tomographic vector of data,  $d_{ij}(\theta)$ , and the two-point functions theoretical predictions,  $v_{ij}(\theta; \gamma)$ , are computed at twenty angular scales, between  $6''$  and  $1'$ , and correlate three redshift bins  $i, j = [1; 3]$ . The covariance matrix of the estimator used to measure the two-point shear statistics,  $C(\theta; \gamma^0; \gamma)$ , has dimension  $120 \times 120$ .

The redshift bins are the ones used in Fig. 4:  $z_1 = [0; 0.77]$ ;  $z_2 = [0.77; 1.15]$ ;  $z_3 = [1.15; 4.0]$ , with mean redshifts of  $z_1 = 0.47$ ;  $z_2 = 0.94$ ;  $z_3 = 1.69$ , respectively. They were chosen such as to optimise the information. Since the signal increases with redshift, it is more efficient to divide the redshift range such that the lower-redshift bins contain a larger fraction of the galaxies. We followed the strategy of Hu (1999) and defined the bins such that  $z_1$  contains half of the galaxies and  $z_2$  and  $z_3$  contain one quarter each. The correlation coefficient between the aperture mass variances of the various bins is defined as  $r_{ij}(\theta) = M_{ap,ij}^2(\theta) / (M_{ap,ii}^2(\theta) M_{ap,jj}^2(\theta))^{1/2}$ . We measure a large correlation  $r_{12} = r_{23} = 0.9$  between consecutive bins, which shows that further subdivisions do not increase the amount of information.

The data vector,  $d_{ij}(\theta)$ , is computed for a fiducial model similar to the WMAP5 average values ( $a_m = 0.27$ ,  $a_c = 0.73$ ,  $b_m =$

0.705,  $\sigma_8 = 0.812$ ,  $\Omega_m = 0$ ) for a  $\Lambda$ CDM cosmology (Dunkley et al. 2008) and no bias.

The value of  $v_{ij}(\mathbf{z})$  depends on cosmological parameters and also on the bias parameters  $a_m, b_m, a_c, b_c$ . The chosen range of the bias parameters covers the results of the STEP2 analysis:  $a_m = [0.03; 0]$ ,  $b_m = [0.06; 0.06]$ ,  $a_c = [0.001; 0]$  and  $b_c = [0.006; 0.002]$ . The cosmological parameters varied in the grid are: the matter density  $\Omega_m = [0.1; 1.0]$ , the Hubble constant  $h = [0.6; 0.8]$ , the normalisation of the matter power spectrum  $\sigma_8 = [0.5; 1.1]$ , and two parameters,  $w_0$  and  $w_1$ , for the equation of state of dark energy,  $w_{DE}(\mathbf{z}) = w_0 + w_1 \log(1+z)$ . We model  $w_{DE}(\mathbf{z})$  in two different ways. The first one is a constant equation of state,  $w_{DE}(\mathbf{z}) = w_0 = \text{const}$ ; for this model we vary  $w_0 = [-2.0; 0]$ . The second model has been suggested by Benabed & van Waerbeke (2004):

$$w_{DE}(\mathbf{z}) = \begin{cases} w_0 + w_1 \log(1+z) & ; z \leq 1 \\ w_0 + w_1 [\log(2) + \arctan(1) + \arctan(z)] & ; z > 1 \end{cases} \quad (12)$$

Benabed & van Waerbeke (2004) have shown this model is able to mimic quite accurately the Universe dynamics generated by SUGRA potentials. For this case we consider the ranges  $w_0 = [-2.0; 0]$ ,  $w_1 = [0; 0.4]$ .

For the source redshift distribution we use the parameterization of Eq. (9). We do not vary its parameters in the likelihood analysis. This choice is supported by the fact that the errors affecting the estimation of the parameters  $\alpha$ ,  $\beta$  and  $z_0$  are about one percent, including the sample variance affecting the CFHTLS-Deep catalogue (van Waerbeke et al. 2006).

## 5 COVARIANCE MATRIX

In this section we compute the covariance matrix  $C(\#_1; \#_2; \mathbf{z})$  for Eq. (11). Most studies of weak lensing tomography have been made in Fourier space where the covariance matrix is easy to compute. Analyses made in real space usually evaluate the covariance matrix from Monte Carlo simulations (eg., Simon, King & Schneider 2004), or more recently analytically from the covariances of power spectra (Joachimi, Schneider & Eifler 2008). Here we follow a different approach deriving analytically in real space  $C_{++} = C(\mathbf{z}_1; \mathbf{z}_2; \mathbf{z})$ , the covariance matrix of  $\mathbf{z}_1; \mathbf{z}_2(\mathbf{z})$ , extending to tomography the formulae derived in Schneider et al. (2002). The details of the derivation are given in appendix A. The covariances of the estimators of  $\mathbf{h}_{ap}^2(\mathbf{z})$  and  $\mathbf{h}^2(\mathbf{z})$  are afterwards derived from the covariance of  $\mathbf{z}_1; \mathbf{z}_2(\mathbf{z})$  (Schneider et al. 2002).

The pure cosmic variance term is analytically derived in Appendix A assuming a Gaussian shear field [Eqs. (A9) and (A10)], for the a fiducial model defined in this case defined in the previous section. We then recalibrate this matrix for non-Gaussian contributions following Semboloni et al. (2007), hereafter S07. This consists in multiplying the Gaussian cosmic variance by a calibration factor  $F(\#_1; \mathbf{z}_1; \#_2; \mathbf{z}_2)$ .

We found that the calibration factor found in S07 needed to be modified for the case of tomography by applying it to Eqs. (A9) and (A10), and comparing the result with the non-Gaussian cosmic variance for tomography, measured directly on the same set of ray-tracing simulations used in S07. The best agreement is obtained when the redshift used in the calibration factor of S07,

$$F(\#_1; \mathbf{z}_1; \#_2; \mathbf{z}_2) = \frac{v(\mathbf{z})}{v(\mathbf{z}_1; \mathbf{z}_2)}; \quad (13)$$

is redefined as an effective redshift  $\mathbf{z} = \mathbf{z}(\mathbf{z}_1; \mathbf{z}_2)$  given by

$$\mathbf{z}(\mathbf{z}_1; \mathbf{z}_2) = \frac{1}{2} \sqrt{(\mathbf{z}_1 + \mathbf{z}_2)(\mathbf{z}_1 + \mathbf{z}_2)}; \quad (14)$$

The effective redshift is thus the geometric mean of the average redshifts of the bins involved in each of the two correlations  $\mathbf{z}_1; \mathbf{z}_2$  and  $\mathbf{z}_1; \mathbf{z}_2$ . The functional form of  $v(\mathbf{z})$  and  $v(\mathbf{z})$  are defined in S07, with the same best-fit parameter values ( $a_1; a_2; a_3; b_1; b_2; b_3; b_4; t_1; t_2; t_3$ ) indicated there. Finally, the recalibration is only applied at angular scales below the  $\theta_{max}$  defined in S07.

We find that this fitting formula agrees with the measured covariance to an accuracy of 20%; the worst result being for the lower redshift bin. This recalibration might overestimate the values of the covariance matrix (Takada & Jain 2008) (as the simulations we used have a high value  $\sigma_8 = 1$ ) but this is not so important as we include in our likelihood analysis large scales measurements.

After recalibrating the cosmic variance term, we add the other contributions to  $C_{++}$ : the coupling between shape-noise and the shear signal given by Eq. (A12), and the pure shape-noise term given by Eq. (A13). These terms depend on the density of galaxies, the total area of the survey and the intrinsic ellipticity dispersion. We assume a density of galaxies integrated along the line of sight of  $n = 12 \text{ arcmin}^{-2}$  which is similar to the CFHTLS-Wide survey with a median redshift of  $z_m = 0.8$ . To find the density of galaxies for each redshift bin, we normalise the redshift distribution of the sources,  $p(\mathbf{z})$ , to  $n$  and integrate it between each  $z_{inf}$  and  $z_{sup}$ . We use an intrinsic ellipticity dispersion  $\epsilon = 0.44$ . The cosmological constraints are derived for two different survey areas:  $A = 170 \text{ deg}^2$  and  $A = 2000 \text{ deg}^2$ , which are a good representation of current and future weak lensing ground-based multicolor surveys. The first case has the same sky coverage and depth as the CFHTLS-Wide survey. The second has similar sky coverage to the upcoming KIDS survey, while being about half a magnitude deeper than KIDS. However, as the shape measurement bias is a function of signal-to-noise, we expect it to be larger, for the same magnitude, in a shallower survey than in a deeper one.

Finally, using Eq. (42) of Schneider et al. (2002) with  $K_+ = 1$ , we obtain the covariance matrix of the estimator of  $\mathbf{h}_{ap}^2(\mathbf{z})$  from  $C_{++}$ , and using a similar expression we derive the covariance matrix of the estimator of  $\mathbf{h}^2(\mathbf{z})$ .

During the likelihood analysis the covariance matrix is kept constant, neglecting its dependence on the cosmological parameters. The accuracy of this approximation is studied in Eifler, Schneider & Hartlap (2008). We also neglect its dependence on bias parameters. Thus in the likelihood defined by Eq. (11), the dependence on the bias is only contained in  $v_{ij}$ . This type of systematic error which affects the signal but does not introduce extra noise in the covariance matrix has been called Type I by Kitching, Taylor & Heavens 2008a and it allows for self-calibration.

## 6 RESULTS

In this section we obtain cosmological constraints by performing the likelihood analyses previously described, both with and without tomography. As stated earlier on, our approach is to include the realistic bias measured in STEP2, with as little extra modeling as possible. For this reason we choose not to model the correlation of the additive term, which does not come directly from the STEP2 analysis. We will focus thus on the multiplicative bias and show constraints using the aperture-mass dispersion only.



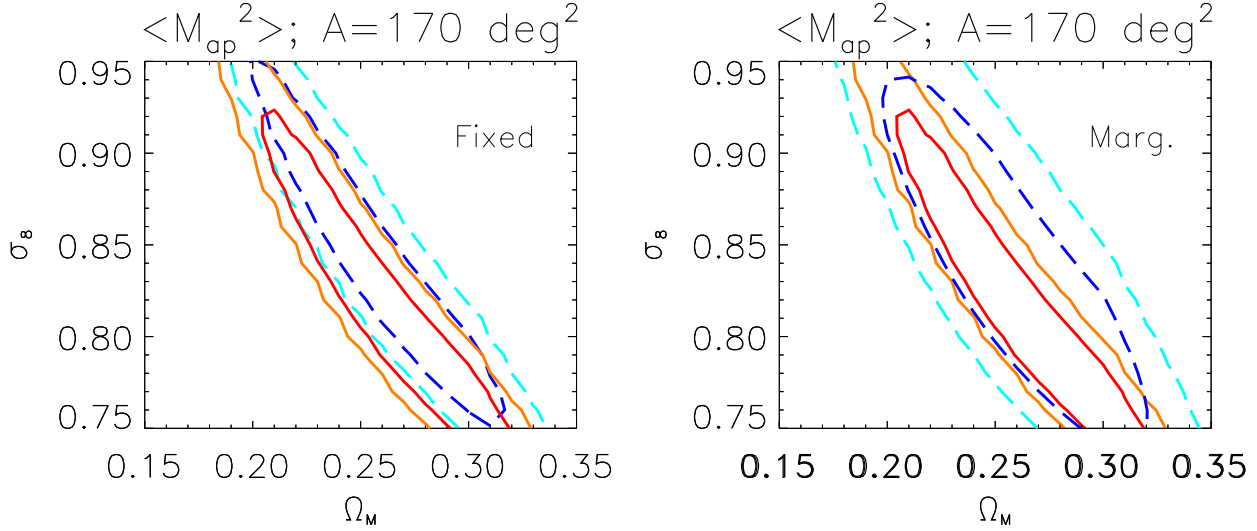


**Figure 5.** Cosmological constraints in the  $[m; s]$  plane for a survey of area  $170 \text{ deg}^2$  and three tomographic bins. The contours represent the 68% and 95% confidence regions and are marginalized over the hidden cosmological parameters. Left panel: the effect of a fixed bias of  $a_m = 0.02; b_m = 0$  (dashed, blue) is compared with the bias-free contour (solid, red). Right panel: the biased contour is now marginalized over the bias parameters (dashed, blue) and compared with the bias-free contour (solid, red).

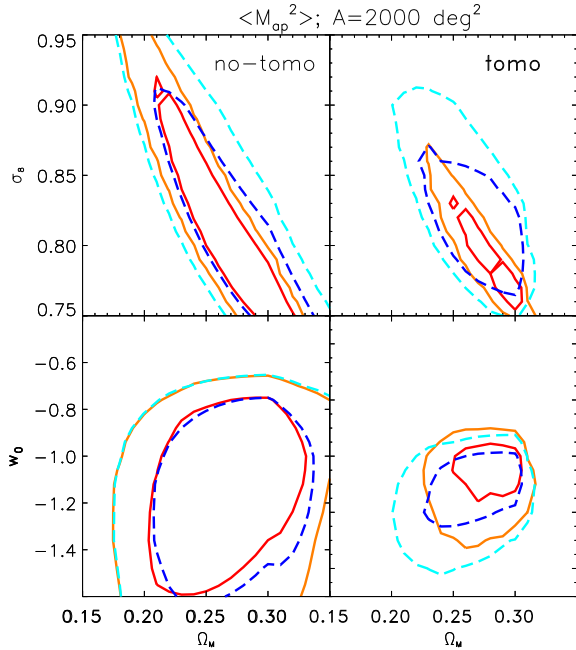


**Figure 6.** Confidence regions (68% and 95%) on the  $[m; w_0]$  and  $[m; s]$  planes for the  $2000 \text{ deg}^2$  survey. The contours, marginalized over the hidden parameters, are shown for the case of no bias (solid, red) and marginalizing over the shape measurement bias parameters (dashed, blue). Left panels show results of the non-tomographic analysis and right panels refer to the tomographic case.

We start by considering the  $170 \text{ deg}^2$  survey, which has relatively large noise, to assess if a redshift-dependent shape measurement bias already affects the results of a tomographic analysis of a survey such as the CFHTLS-Wide. The constraints in the  $[m; s]$  plane, using auto- and cross-correlation in the three redshift bins previously described, are shown in Figure 5. In the left panel, con-

tours are shown for the case of no bias and a particular choice of bias ( $a_m = 0.02; b_m = 0$ ). The biased contour is clearly shifted to the upper-right corner to compensate the negative multiplicative bias. This shows that our choice of redshift binning is quite effective, having a noise level low enough for systematics to become important. The shift in the constraints can be quantified by fitting the direction of the degeneracy seen in the plot. In the case of no bias the fit is given by

$$s(m=0.275)^{0.48} = 0.79 \pm 0.02; \quad (15)$$

whereas in the case of this particular bias we find

$$s(m=0.275)^{0.43} = 0.81 \pm 0.02; \quad (16)$$

This result shows that ignoring the presence of the shape measurement bias would lead to biased contours.

When the amplitude of the bias is not known, the safer approach is to marginalize over a reasonable interval of bias. Marginalizing over the range suggested by our STEP2 analysis, we find the contour shown in Figure 5 (right panel). The precision of the tomographic measure of  $[m; s]$  is reduced by a factor of 2. This result includes the degeneracies between cosmological and bias parameters. Marginalizing over the cosmological parameters, the bias parameters could be estimated from the data, i.e., the signal could be self-calibrated. For the self-calibration to be effective, priors would be needed. They can be obtained with extra information from independent measurements affected by the same systematics. Other measures of cosmic shear such as higher-order correlation functions (Bernardeau, van Waerbeke & Mellier 1997) or the shear-ratio test (Jain & Taylor 2003) could be helpful for this purpose.

Finally, we also produced contours in the  $[w_0; m]$  plane. In this case the systematics do not have a relevant effect, since the bias-free contours are too broad and the estimate is noise-dominated.

We turn now to the case of the survey of  $A = 2000 \text{ deg}^2$ , in order to see how the shape measurement bias can affect the weak lensing analysis of data from future ground-based observations. We quantify the constraints using a figure-of-merit, FoM, defined as the



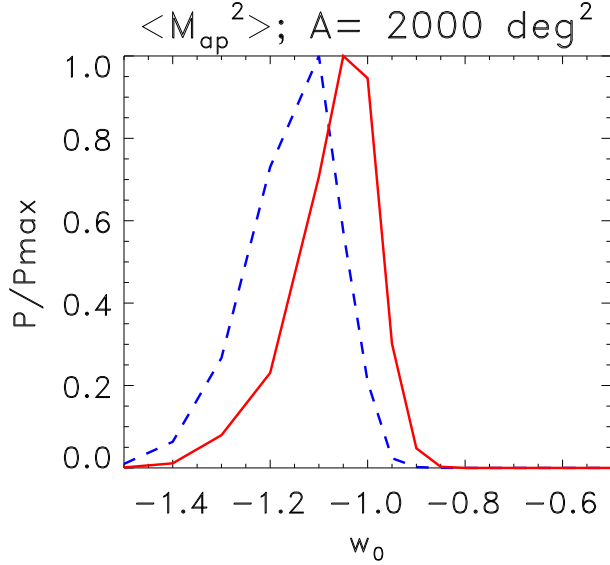


**Figure 7.** Marginalised 1-dimensional probability distribution of  $w_0$  for two cases: no bias (solid line, red) and a shape measurement bias characterized by  $a_m = 0.02$ ,  $b_m = 0$  (dashed line, blue), for the  $A=2000 \text{ deg}^2$  survey. The peak of the probability distribution changes significantly with the shape measurement bias parameters.

inverse of the area enclosed by the 68% confidence level. Quoted results imply a marginalisation of the bias over its full range.

In Figure 6, we show the cosmological constraints in the  $[m; \delta]$  and  $[m; w_0]$  planes, both for tomography and non-tomography, using the variance of the aperture mass. The first interesting result is that tomography produces an enormous gain in all constraints, but especially in dark energy. Looking at the bias-free contours, the increase in the FoM between using and not using tomography is a factor of 10 for the  $[m; w_0]$  contour and a factor of 6 for  $[m; \delta]$ . This is larger than the improvement between the two surveys due to the increase in area, which scales with the square root of the survey area and is thus around 3.5.

Regarding the impact of the bias, we find the multiplicative redshift-dependent bias essentially does not affect the non-tomographic constraints, even for a KIDS-like survey. Indeed, the FoM of the  $[m; w_0]$  contour only decreases by a factor of 1.1 in the presence of bias. For the  $[m; \delta]$  contour the decrease is larger, around 1.6. The tomographic constraints are however more strongly affected by the bias. We find using tomography the  $[m; \delta]$  marginalised FoM is 3.5 smaller in comparison to the tomographic FoM without bias. It is still better than the bias-affected non-tomographic one by a factor of around 2, but it is only slightly better than to FoM for the  $A = 170 \text{ deg}^2$  survey in the case of no-bias. Notice however that even though the two FoM are similar, the corresponding one-dimensional constraints for  $m$  and  $\delta$  are different. Indeed the two contours (the solid contour in the right panel of Fig. 5 and the dashed one in the upper-right panel of Fig. 6) have different shapes. This indicates the effect of the bias is not equivalent to an increase of the data error bars. Similarly, marginalising over the bias causes the FoM of the tomographic  $[m; w_0]$  constraint to increase by a factor of 2 in comparison to the unbiased FoM.

The finding that tomography is more affected by the bias reflects the fact that cosmological and bias parameters are more correlated for this case. We looked at the bias-cosmology correlations and verified that while for the non-tomographic case only  $m$

shows some correlation with  $a_m$  and  $b_m$ , in the case of tomography  $m$ ,  $\delta$  and  $w_0$  are all correlated with  $a_m$ . In particular,  $\delta$  and  $a_m$  are anti-correlated, whereas  $w_0$  and  $a_m$  correlate. This means a lower (more negative)  $w_0$  is needed to compensate the multiplicative bias, which essentially underestimates the signal. This result can be explained if one considers how the properties of large-scale structures depends on dark energy. For larger  $w_0$ , dark energy starts to dominate at times later than those predicted by  $\Lambda$ CDM, and the structures grow faster. If one normalises the amplitude of the density fluctuations to the present time then models with  $w_0 > -1$  would have less structure in the past and produce a signal  $\Delta M_{ap}^2(\#)$  which is smaller than the signal produced by the  $\Lambda$ CDM model. The dark energy affects two-point cosmic shear statistics also via the geometric factor and this effect has the opposite result increasing the amplitude of  $\Delta M_{ap}^2(\#)$  with  $w_0$  (Simpson & Bridle 2005). This last effect is dominant for the correlations involving the lower redshift bins, whereas the previous effect is dominant for high redshift bins. For our particular choice of redshift bins, the first effect is the dominant one, as is shown in Figure 7, by the shift to the left of the probability distribution, in the presence of bias. This plot also illustrates that ignoring the presence of a shape measurement bias on the likelihood analysis may lead to an incorrect cosmological interpretation.

We also performed a likelihood analysis for the  $A = 2000 \text{ deg}^2$  survey, this time using the equation of state of dark energy given by Eq. (12), including an extra parameter,  $w_1$ . The resulting marginalised contours for both the  $[m; \delta]$  and the  $[m; w_0]$  plane are very similar to the results of the previous analysis. The left panel of Figure 8 shows the contours in the  $[w_0; w_1]$  plane. They are weakly affected by the bias, broadening mildly towards lower values of  $w_0$  consistently with the previous analysis.  $\Delta M_{ap}^2(\#)$  cannot independently measure  $w_1$ , as shown by the rather flat probability distribution in the right panel of Figure 8 (solid line). However for a bias of ( $a_m = 0.02$ ;  $b_m = 0$ ), i.e., assuming this bias in the theoretical models and keeping the fiducial model bias-free, the probability distribution is much narrower. The reason for this is that the impact of this bias on the models is much larger than the effect of  $w_1$ . Therefore, most values of  $w_1$  cannot compensate for the bias impact. Conversely, when doing a likelihood analysis of real data biased by an unknown amount, assuming no bias in the theoretical models, the same effect may occur leading to an inaccurate but apparently precise estimate.

## 7 CONCLUSIONS

We have investigated the impact of realistic redshift-dependent measurement bias on the estimation of cosmological parameters using two-point shear statistics in a tomographic approach with three redshift bins. We focused on two survey types of the same depth, with median redshift 0.8, covering an area of  $170 \text{ deg}^2$  and  $2000 \text{ deg}^2$ , representing current and near-future ground-based weak lensing surveys, respectively.

We performed a likelihood analysis in a grid of cosmological and bias parameters. The covariance matrix of the tomographic two-point functions was derived analytically in the real space, extending the formulae of Schneider et al. (2002), and was afterwards calibrated for non-Gaussianity, extending the fitting formula of Semboloni et al. (2007).

Realistic redshift-dependent multiplicative bias were obtained reanalyzing the STEP2 set of simulations with a KSB pipeline. The results of our analysis are thus strictly valid for KSB-based mea-

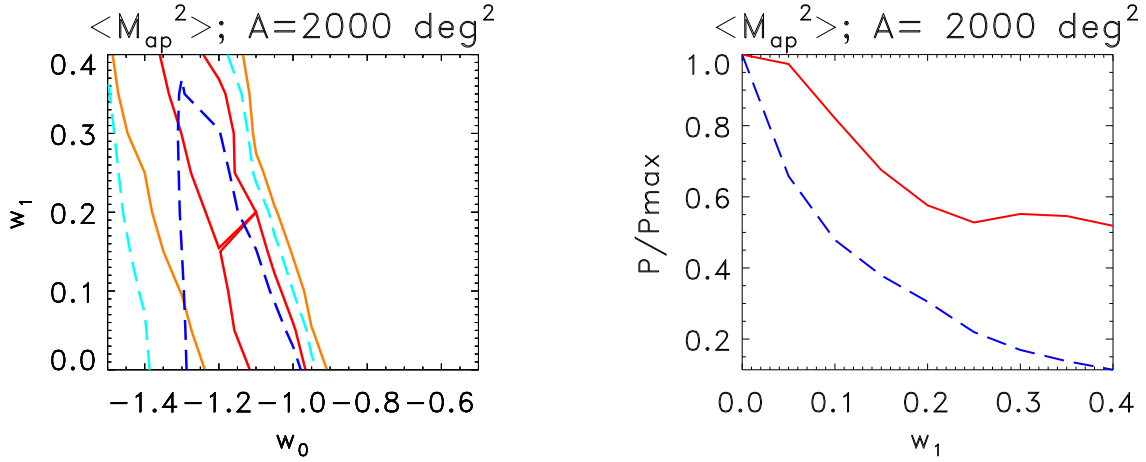


**Figure 8.** Cosmological constraints on the parameters of the dark energy equation of state, for the survey of area  $A = 2000 \text{ deg}^2$ . Left panel: 68% and 95% confidence regions on the  $[w_0, w_1]$  plane for the non-bias case (solid, red) and marginalised over the bias parameter space (dashed, blue). Right panel: the marginal 1-dimensional probability distribution for  $w_1$  obtained assuming no bias (solid line, red) and assuming a fixed bias of  $(a_m = 0.02; b_m = 0)$  (dashed line, blue).

measurements only. In this framework, our results are also a worst-case scenario, since the higher end of the bias values found correspond to the highly elliptical PSFs D and E of STEP2, which will be avoided by design in future surveys. Nevertheless, such ellipticities are comparable with those measured in the outer regions of CFHTLS-Wide fields.

The top-hat variance is more sensitive to the presence of a shape measurement bias than the variance of the aperture mass. In particular, in the case of a large scale-independent additive bias, cosmological interpretation of the signal may even not be possible, suggesting that aperture mass statistics should be preferred to top-hat statistics. The measurement of  $\bar{M}_{\text{ap}}^2(\#)$  is however also quite sensitive to the shape measurement bias; its amplitude is reduced by 20% at redshift 1, and its scaling with redshift becomes shallower.

We stress the results shown in this paper are based only on the simulations. Using these simulations the aperture mass variance seems to be more accurate than the top-hat variance, this because the top-variance is particularly sensitive to the additive bias as long as this bias is constant across the field. On real data this is not often true and we expect both two-point shear statistics to be biased. Unfortunately, we could not quantify this effect using this set of simulations as the PSF is constant across the field. Moreover, in real data, the profile of the PSF is not constant in time, space and color, and it might have a more complex shape. These factors may introduce other sources of bias which are not investigated here. Finally, in real data, the lack of accuracy on the estimation of photometric redshifts could further decrease the scaling of the two-point shear statistics with redshift. Indeed, the presence of outliers in photometric redshift estimation is known to decrease the measured slope of the evolution of the cosmic shear signal (Erben et al. 2008).

We found the redshift-dependent bias to have, in general, a large impact on the tomographic measurements. For example, constraints obtained from the largest survey, marginalised over the realistic bias interval, are comparable to the ones from the ten times smaller survey assuming the latter does not suffer from measurement bias.

Ignoring the presence of a shape measurement bias can all-bias the estimation of cosmological parameters in surveys

such as the CFHTLS-Wide. From our analysis, the bias on  $\beta$  is of a few percent. For the survey of  $2000 \text{ deg}^2$  the effect of ignoring the bias is more important, around 5%, corresponding roughly to 1%, for  $w_0$ , and larger for  $w_1$ .

The safer approach when dealing with unknown biases is to marginalise over a realistic range. While this reduces the constraining power of the tomographic analysis over a non-tomographic one, there is the possibility for self-calibrating by combining information from other cosmic shear measures. However, the best approach would be to correct for these biases. For such a reason, collaborations that aim to improve the measurement of the galaxy shapes such as STEP and GREAT08 (Bridle et al. 2008) are important for the development and improvement of shear measurement methods. As an example, the simulations produced by the STEP collaboration have been used to develop and test new PSF-correction methods, such as shapelets-based decompositions (Kuijken 2006) and the LENSFIT method (Kitching et al. 2008b), which are among the most promising methods for future weak lensing analysing.

To conclude, this analysis, which is limited to the KSB PSF correction method and uses only the STEP2 set of simulations shows the importance to investigate further the dependence of the shear measurement bias on the simulated galaxy properties in order to infer more accurate constraints on cosmological parameters. Furthermore, simulations cannot be used to investigate all the sources of systematic errors which may be present on real data; for this reason one needs to complement this study using consistency tests with real data, for example measuring the cosmic shear signal of various galaxy populations with different color, size, magnitude and ellipticity.

## 8 ACKNOWLEDGMENTS

We warmly thank the participants of the STEP collaboration, in particular we would like to thank Richard Massey for producing and making available the set of simulations used for this paper. We also thank the participants of the CFHTLS Systematics collaboration for helpful comments. We are grateful to Peter Schneider and Thomas Erben for a careful reading of the manuscript. ES acknowledges the

support of the Alexander von Humboldt foundation. IT acknowledges the support of the European Commission Programme 6-th framework, Marie Curie Training and Research Network “DUEL”, contract number CT-2006-036133.

Takada M., Jain B., 2008, MNRAS, submitted, pre-print arXiv:0810:4170  
 van Waerbeke L. et al., 2001, A&A, 347, 757  
 van Waerbeke L., Mellier Y., Hoekstra H., 2005, A&A, 429, 75  
 van Waerbeke L., White M., Hoekstra H., Heymans C., 2006, APh, 26, 91

## REFERENCES

- Albrecht A. et al., 2006, pre-print arXiv:astro-ph/0609591  
 Amara A., Réfrégier A., 2007, MNRAS, 381, 101  
 Bartelmann M., Schneider P., 2001, Phys. Rep., 340, 291  
 Benabed K., van Waerbeke L., 2004, Phys. Rev. D, 70, 12  
 Benjamin J. et al., 2008, MNRAS, 381, 702  
 Bernardeau F., van Waerbeke L., Mellier Y., 1997, A&A, 322, 1  
 Bernstein G., Jarvis M., 2002, AJ, 123, 583  
 Bridle S., King L., 2007, NJPh, 9, 444  
 Bridle S. et al., 2008, pre-print arXiv:0802:1214  
 Crittenden R., Natarajan, P., Pen U., Theuns, T., 2001, ApJ,  
 Dunkley J. et al., 2008, ApJS submitted, pre-print arXiv:0803.0586  
 Eifler T., Schneider, P., Hartlap, J., 2008, A&A submitted, pre-print  
 arXiv:0810.4254  
 Erben T. et al., 2008, A&A accepted, pre-print arXiv:0811.2239  
 Fu L. et al., 2008, A&A, 479, 9  
 Heymans C. et al., 2006a, MNRAS, 368, 1323  
 Heymans C., White M., Heavens A., Vale C., van Waerbeke L., 2006b, MNRAS, 371, 750  
 Hirata C., Seljak U., 2003, MNRAS, 343, 459  
 Hirata C., Seljak U., 2004, Phys. Rev. D, 70, 6  
 Hirata C., Mandelbaum R., Ishak M., Seljak U., Nichol R., Pimbblet K.,  
 Ross N., Wake D., 2007, MNRAS, 38, 1197  
 Hoekstra, H., 2004, MNRAS, 347, 1337  
 Hoekstra H. et al., 2006, ApJ, 347, 116  
 Hu W., 1999, ApJ, 522, 21  
 Huterer D., Takada M., Bernstein G., Jain B., 2006, 366, 101  
 Ilbert O. et al., 2006, A&A, 457, 841  
 Ishak M., Hirata C., 2005, Phys. Rev. D, 71, 023002  
 Jain B., Taylor A., 2003, Phys. Rev. Lett., 91, 141302  
 Jain B., Jarvis M., Bernstein G., 2006, JCAP, 2, 1  
 Jarvis M., Bernstein G., Jain B., Dolney D., 2006, ApJ, 644, 71  
 Joachimi B., Schneider P., Eifler, T., 2008, A&A, 477, 43  
 Kaiser N., Squires J., Broadhurst T., 1995, ApJ, 449, 460  
 Kilbinger M. et al., 2008, A&A submitted, pre-print arXiv:0810.5129  
 Kitching T. D., Taylor A. N., Heavens, A. F., 2008a, MNRAS, 389, 173  
 Kitching T.D., Miller L., Heymans C., van Waerbeke L., Heavens A.,  
 2008b, MNRAS, 390, 149  
 Kuijken K., 2006, A&A, 456, 827  
 Luppino G., Kaiser N., 1997, ApJ, 475, 20  
 Ma Z., Hu W., Huterer D., 2006, ApJ, 636, 21  
 Mandelbaum R., Hirata C., Ishak M., Seljak U., Brinkmann J., 2006, MNRAS, 367, 611  
 Massey R., Réfrégier A., Conselice C., Bacon D., 2004, MNRAS, 348, 214  
 Massey R. et al., 2007, MNRAS, 376, 13  
 Munshi D., Valageas P., van Waerbeke L., Heavens A., 2008, Phys. Rep.,  
 462, 67  
 Paulin-Henriksson S., Amara A., Voigt L., Réfrégier A., Bridle S., 2008,  
 A&A, 484, 67  
 Peacock J. A. et al., 2006, Messenger, 125, 48  
 Réfrégier A., Bacon D., 2003, MNRAS, 338, 48  
 Schimd C. et al., 2007, A&A, 463, 405  
 Schneider P., van Waerbeke L., Kilbinger M., Mellier Y., 2002, A&A, 396,  
 1  
 Semboloni E. et al., 2006, A&A, 452, 51  
 Semboloni E., van Waerbeke L., Heymans C., Hamana T., Colombi S.,  
 White M., Mellier Y., 2007, MNRAS, 375, L6  
 Simon P., King L., Schneider P., 2004, A&A, 417, 873  
 Simpson F., Bridle S., 2005, Phys. Rev. D, 71, 083501  
 Takada M., Jain B., 2004, MNRAS, 348, 897

## APPENDIX A: COVARIANCE OF THE TOMOGRAPHIC ESTIMATOR OF $\gamma_+$

We extend the calculations of Schneider et al. (2002) (S02 hereafter) in order to explicitly include the redshift binning of the correlation function. Note latin subscripts ( $i, j$ ) refer to individual galaxies, while greek subscripts ( $\alpha, \beta$ ) refer to bins.

The shear  $\gamma_i$  at angular position  $\mathbf{i}$  of a source galaxy at redshift  $z_i$  is estimated from the observed ellipticity of the galaxy image. After deconvolving the PSF, the corrected ellipticity  $e_i$  is related to the intrinsic ellipticity  $s_i$  and the shear by

$$e_i = \frac{s_i}{1 + \gamma_i(Z_i)} : \quad (A1)$$

The correlation function  $\gamma_+(\#; Z(\alpha; \beta))$  between redshift bins with source redshift distributions  $p_\alpha(z)$  and  $p_\beta(z)$  is estimated in angular-separation bins  $\#$ . The angular bins are defined by the function  $\delta_\#(j_i - j_j) = 1$  for  $\# = 2 < j_i - j_j \leq 6 + \# = 2$  and zero otherwise, while the redshift bins are defined by  $\delta_Z(z_i; z_j) = 1$  for  $p_\alpha(z_i) p_\beta(z_j) \neq 0$  and zero otherwise. In other words, only pairs of galaxies with one of the galaxies belonging to the bin  $\alpha$  and the other to the bin  $\beta$  contribute to the correlation at  $Z(\alpha; \beta)$ . The estimator used for the correlation function is,

$$\hat{\gamma}_+(\#; Z) = \frac{\sum_{ij} w_i w_j (\gamma_{i+} + \gamma_{j+} - \gamma_{ij}) \delta_\#(j_i - j_j) \delta_Z(z_i; z_j)}{N_p(\#; Z)} ; \quad (A2)$$

where the subscripts  $(+)$  refer to the two components of the ellipticity,  $N_p(\#; Z)$  is the effective number of pairs contributing to the correlation at  $(\#; Z)$  and  $w_i, w_j$  allow for weighting the galaxies. In the absence of intrinsic alignments and shear-shape correlations, Eq. (A2) is an unbiased estimator of  $\gamma_+$ . The noise of the estimator is a function of the ellipticity shape noise,  $\langle \frac{s_{i+} s_{j+}}{1 + \gamma_i} + \frac{s_i s_j}{1 + \gamma_j} \rangle = \sigma_{ij}^2$ , which we assume is independent of redshift.

The covariance of  $\hat{\gamma}_+(\#; Z)$  is defined as

$$\text{Cov}(\hat{\gamma}_+; \#_1; Z_1; \hat{\gamma}_+; \#_2; Z_2) = \langle \hat{\gamma}_+(\#_1; Z_1) \hat{\gamma}_+(\#_2; Z_2) \rangle - \gamma_+(\#_1; Z_1) \gamma_+(\#_2; Z_2) : \quad (A3)$$

Inserting Eq. (A2) it reads,

$$\begin{aligned} \text{Cov}(\hat{\gamma}_+; \#_1; Z_1; \hat{\gamma}_+; \#_2; Z_2) &= \frac{\sum_{ijkl} w_i w_j w_k w_l \delta_{\#_1}(ij) \delta_{\#_2}(kl) \delta_{Z_1}(ij) \delta_{Z_2}(kl) h(i_1 j_1 + i_2 j_2)(k_1 l_1 + k_2 l_2)}{N_p(\#_1; Z_1) N_p(\#_2; Z_2)} \\ &\quad + \gamma_+(\#_1; Z_1) \gamma_+(\#_2; Z_2) : \end{aligned} \quad (A4)$$

This expression depends on four-point correlations involving the four positions  $(i; z_i)$ ,  $(j; z_j)$ ,  $(k; z_k)$  and  $(l; z_l)$ , where the first two positions define  $(\#_1; Z_1)$  and the latter two define  $(\#_2; Z_2)$ . In order to evaluate it, we proceed as in S02: inserting Eq. (A1); assuming a Gaussian shear field and thus factoring four-point functions as a sum over products of two-point functions (assuming no intrinsic alignments), and finally writing the two-point correlations of the shear components as function of  $\gamma_+$  and  $\gamma_{ij}$ . We obtain the results (A5)-(A7), which differ from Eq. (23) of S02 since we can no longer interchange  $i$  with  $j$  or  $k$  with  $l$  which may have different redshifts. The cosmic variance term reads

$$\begin{aligned} V_{++}(\hat{\gamma}_+; \#_1; \hat{\gamma}_+; \#_2) &= \frac{1}{N_p(\#_1; Z_1) N_p(\#_2; Z_2)} \frac{1}{2} \sum_{ijkl} w_i w_j w_k w_l \delta_{\#_1}(ij) \delta_{\#_2}(kl) \delta_{Z_1}(ij) \delta_{Z_2}(kl) \left[ + (i_1 l_1) + (j_1 k_1) + \right. \\ &\quad \left. + (i_2 l_2) + (j_2 k_2) + \cos[4(\theta_{i_1} - \theta_{j_1})] (i_1 l_1) (j_1 k_1) + \cos[4(\theta_{i_2} - \theta_{j_2})] (i_2 l_2) (j_2 k_2) \right] ; \end{aligned} \quad (A5)$$

where  $\theta_{ij}$  is the polar angle of the vector  $\mathbf{i} - \mathbf{j}$ . The mixed term, with the coupling between shape-noise and shear, is now

$$\begin{aligned} M_{++}(\hat{\gamma}_+; \#_1; \hat{\gamma}_+; \#_2) &= \frac{1}{N_p(\#_1; Z_1) N_p(\#_2; Z_2)} \frac{1}{2} \left[ \sum_{ijk} w_i^2 w_j w_k \delta_{\#_1}(ij) \delta_{\#_2}(ik) \delta_{Z_1}(ij) \delta_{Z_2}(ik) + (jk) + \right. \\ &\quad + \sum_{ijk} w_i w_j^2 w_k \delta_{\#_1}(ij) \delta_{\#_2}(jk) \delta_{Z_1}(ij) \delta_{Z_2}(jk) + (ik) + \sum_{ijl} w_i^2 w_j w_l \delta_{\#_1}(ij) \delta_{\#_2}(il) \delta_{Z_1}(ij) \delta_{Z_2}(il) + (jl) + \\ &\quad \left. + \sum_{ijl} w_i w_j^2 w_l \delta_{\#_1}(ij) \delta_{\#_2}(jl) \delta_{Z_1}(ij) \delta_{Z_2}(jl) + (il) \right] : \end{aligned} \quad (A6)$$

The noise term is similar to the non-tomographic case, only contributing to the diagonals of the covariance matrix, i.e. for  $\#_1 = \#_2$  and  $Z_1 = Z_2$ . It reads,

$$S_{++}(\hat{\gamma}_+; \#_1; \hat{\gamma}_+; \#_2) = \frac{1}{N_p(\#_1; Z_1) N_p(\#_2; Z_2)} \sum_{ij} w_i^2 w_j^2 \delta_{\#_1}(ij) \delta_{\#_2}(ij) \delta_{Z_1}(ij) \delta_{Z_2}(ij) : \quad (A7)$$

Table A summarizes the dependence of the cosmic variance on the tomographic auto- and cross-correlation functions, considering two redshift bins for illustration purposes. In the case the cross-correlation signal is not considered in the data vector, the matrix reduces to the sub-matrix highlighted, which nonetheless depends on the tomographic cross-correlation. Note this restricted case corresponds to imposing  $p_\alpha(z) = p_\beta(z)$  being thus invariant under  $i \leftrightarrow j$  and  $k \leftrightarrow l$  transformations, and therefore Eqs. (A5)-(A7) reduce to Eq. (23) of S02.

	11	22	12
11	11 11 + S	12 12	j
22	12 12	22 22 + S	j
12	11 12	22 12	11 22 + 12 12 + S

**Table A1.** Summary of the tomographic cosmic variance matrix, with dimension  $3 \times 3$  corresponding to 2 redshift bins ( $z = [1; 2]$ ), showing the dependence on the various correlation functions  $\xi_+(\#; Z_1; Z_2)$  (denoted by  $\xi$ ). The terms affected by shot noise are also indicated (with S). Dashed lines isolate the restricted case of neglecting the information in the cross-correlation of redshift bins.

The calculations in Eqs. (A5)-(A7) are time-consuming and survey-dependent since they involve sums over the galaxies positions. Still following S02, we calculate a more convenient quantity: the ensemble average of the covariance matrix for a survey of area  $A$  and galaxy density  $n$ , and write the result in the form

$$E \left( \text{Cov}(\hat{\alpha}_+; \#_1; Z_1; \hat{\alpha}_+; \#_2; Z_2) \right) = D_{\#_1 \#_2} (Z_1, Z_2) + \mathcal{Q}_+ + \mathcal{R}_{+0} + \mathcal{R}_{+1}; \quad (\text{A8})$$

For the cosmic variance we obtain

$$\mathcal{R}_{+0} = \frac{1}{A} \int_0^1 d \left[ \int_0^2 d'_{1+;12}(\mathbf{j}_a) \int_0^2 d'_{2+;12}(\mathbf{j}_b) + \int_0^2 d'_{1+;12}(\mathbf{j}_a) \int_0^2 d'_{2+;12}(\mathbf{j}_b) \right]; \quad (\text{A9})$$

$$\begin{aligned} \mathcal{R}_{+1} &= \frac{1}{(4\pi)A} \int_0^1 d \int_0^2 d'_{1+;12}(\mathbf{j}_a) \int_0^2 d'_{2+;12}(\mathbf{j}_b) [\cos 4'_a \cos 4'_b + \sin 4'_a \sin 4'_b] \\ &+ \frac{1}{(4\pi)A} \int_0^1 d \int_0^2 d'_{1+;12}(\mathbf{j}_a) \int_0^2 d'_{2+;12}(\mathbf{j}_b) [\cos 4'_a \cos 4'_b + \sin 4'_a \sin 4'_b]; \end{aligned} \quad (\text{A10})$$

where  $_{+;}$  is a short-hand notation for  $_{+}(\#; Z_1; Z_2)$ . The result was obtained as in S02: the integrations arise from the averaging operator, and a change of variable is made from the position angles  $\theta$ , included in Eq. (A5), to separation angles  $\theta'$ . We note that due to the loss of the  $i, j, k$  invariances, different changes of variables are needed for the two terms of  $\mathcal{R}_{+0}$  or  $\mathcal{R}_{+1}$ ;  $\theta'$  is defined as  $\theta' = \theta_3 - \theta_1$  in one case and  $\theta' = \theta_3 - \theta_2$  in the other. The angular separation information is contained in the vectors  $\mathbf{a}$ ,  $\mathbf{b}$  and their polar angles  $\theta'_a$  and  $\theta'_b$ :

$$\mathbf{a} = \begin{pmatrix} \cos \theta'_a & \#_1 \cos \theta'_{a1} \\ \sin \theta'_a & \#_1 \sin \theta'_{a1} \end{pmatrix}; \quad \mathbf{b} = \begin{pmatrix} \cos \theta'_b + \#_2 \cos \theta'_{b2} \\ \sin \theta'_b + \#_2 \sin \theta'_{b2} \end{pmatrix} \quad (\text{A11})$$

For the mixed term we find

$$\begin{aligned} \mathcal{Q}_+ &= \frac{1}{2A} \int_0^1 d' \left[ \frac{2}{n_1 n_2} \xi_{+;12} \left( \sqrt{\#_1^2 + \#_2^2 - 2\#_1\#_2 \cos \theta'} \right) + \frac{2}{n_1 n_2} \xi_{+;12} \left( \sqrt{\#_1^2 + \#_2^2 - 2\#_1\#_2 \cos \theta'} \right) + \right. \\ &\left. + \frac{2}{n_1 n_2} \xi_{+;12} \left( \sqrt{\#_1^2 + \#_2^2 - 2\#_1\#_2 \cos \theta'} \right) + \frac{2}{n_1 n_2} \xi_{+;12} \left( \sqrt{\#_1^2 + \#_2^2 - 2\#_1\#_2 \cos \theta'} \right) \right]; \end{aligned} \quad (\text{A12})$$

The expectation value of the shot noise term is

$$D = \frac{1}{A 4\pi \#_1 \#_2} \left[ \frac{2}{n_1 n_2} \frac{2}{n_1 n_2} + \frac{2}{n_1 n_2} \frac{2}{n_1 n_2} \right]; \quad (\text{A13})$$

where  $\#$  is the angular bin size. We assume  $\frac{2}{n_1 n_2} = \frac{2}{n_1 n_2} = \frac{2}{n_1 n_2} = \frac{2}{n_1 n_2} = \frac{2}{n_1 n_2}$

Finally, we insert Eq. (A8) in Eq. (42) of S02 to obtain the covariance matrices for the aperture-mass and top-hat dispersion. In the absence of B-modes they depend only on the covariance of  $\alpha_+$ , hence we do not calculate  $\text{Cov}(\hat{\alpha}_+; \hat{\alpha}_+)$  or  $\text{Cov}(\hat{\alpha}_+; \hat{\alpha}_+)$ .